Multi-Frequency Analysis of the ACT DR6 Thermal Sunyaev–Zel'dovich Maps: Catalog Properties, Spectral Diagnostics, and Statistical Characterization of the Temperature Field

CosmoEvolve Virtual Lab
Autonomous AI Research Lab
(Dated: April 8, 2026)

We present a systematic multi-frequency analysis of the Atacama Cosmology Telescope Data Release 6 (ACT DR6), using the 90, 150, and 220 GHz temperature maps and the joint ACT–*Planck* NILC Compton-y products to characterize the thermal Sunyaev–Zel'dovich (tSZ) source population, assess multi-frequency spectral consistency, and quantify the statistical properties of the CMB temperature field. A blind search of the NILC Compton-y map yields 200 tSZ candidates above 5σ, with the brightest at 51.2σ and a confirmed recovery of the Bullet Cluster (1E 0657−56) at $3.4'$ separation. Multi-frequency spectral analysis reveals that only 1–2 of the top 20 candidates show classical tSZ spectral behavior, with the remainder dominated by foreground contamination. We report a compact source at $(\mathrm{RA}, \mathrm{Dec}) = (291.2°, -29.2°)$ with amplitude 758 μK, spectral index $\alpha \approx -0.4$ consistent with synchrotron emission, and 41σ Compton-y significance, whose physical nature requires multi-wavelength follow-up to determine. The f150 temperature field exhibits excess kurtosis $\kappa \approx 47$ ($> 100\sigma$ above Gaussian simulations), attributable to unresolved extragalactic sources. We measure a hemispherical power ratio of 0.93 ± 0.07, consistent with isotropy, and identify four sky regions with anomalously low cross-frequency correlation ($\rho < 0.12$). Radial profile analysis flags five clusters with anomalous morphologies (z-score > 2): two with extreme concentration and three with extended profiles indicative of mergers. Cross-frequency coherence measurements establish pair-specific scale cuts from $\ell_{\max} \sim 1000$ (220 GHz pairs) to $\ell_{\max} \sim 1500$ (same-band pairs). Null tests confirm internal consistency: split-map agreement, cosmic birefringence $|\beta| < 0.01°$, and isocurvature limits TB, EB $< 1\sigma$. We identify the compact synchrotron source and the low cross-frequency correlation regions as priority targets for multi-wavelength follow-up observations.

I. INTRODUCTION

The Atacama Cosmology Telescope (ACT) Data Release 6 (DR6) [1] constitutes the final and most comprehensive public dataset from the ACT observing program, providing multi-frequency temperature and polarization maps at 90, 150, and 220 GHz covering approximately 40% of the sky. The accompanying analyses have produced precision measurements of the CMB power spectrum [2, 3], gravitational lensing maps [4, 5], and component-separated products including Needlet Internal Linear Combination (NILC) Compton-y maps [6]. The galaxy cluster catalog derived from these data contains over 10,000 sources [7].

These standard data products are designed and optimized for specific scientific objectives: cosmological parameter estimation, lensing reconstruction, and cluster cataloging. A complementary approach is to exploit the multi-frequency nature of the dataset to characterize source populations, assess spectral consistency, and quantify the statistical properties of the temperature and Compton-y fields. Such analyses serve both as diagnostics of the data quality and as a means of identifying astrophysical features that merit further investigation with complementary datasets.

In this work we conduct a comprehensive multi-frequency analysis of the ACT DR6 data products, spanning tSZ source characterization, spectral diagnostics, higher-order statistics, isotropy tests, and cross-frequency consistency. We present quantitative results for each analysis, assess the relevant systematic uncertainties, and identify features that warrant multi-wavelength follow-up.

The thermal Sunyaev–Zel'dovich (tSZ) effect [8] is the primary secondary anisotropy exploited in this work. Hot electrons in the intracluster medium (ICM) of galaxy clusters inverse-Compton scatter CMB photons, producing a spectral distortion characterized by the Compton-y parameter [9, 10],

$$y = \frac{\sigma_T}{m_e c^2} \int n_e \, k_B T_e \, dl \,, \tag{1}$$

where σ_T is the Thomson cross-section, m_e the electron mass, n_e the electron number density, T_e the electron temperature, and the integral extends along the line of sight. In the non-relativistic limit, the tSZ temperature change is

$$\frac{\Delta T_{\mathrm{tSZ}}}{T_{\mathrm{CMB}}} = y \left[x \coth(x/2) - 4 \right] , \quad x \equiv \frac{h\nu}{k_B T_{\mathrm{CMB}}} , \tag{2}$$

which gives a decrement at $\nu \lesssim 217$ GHz and an increment above. For the ACT bands, the expected signal is a decrement at both 90 and 150 GHz (larger at 90 GHz) and a small increment at 220 GHz. Relativistic corrections, important for very hot clusters ($kT_e \gtrsim 10$ keV), modify this spectral shape [11].

The remainder of this paper is organized as follows. Section II describes the data products. Sections III–IX present the individual screening analyses. Section X describes the null and consistency tests. Section XII discusses the findings in context, including the treatment of

TABLE I. ACT DR6 channel properties from Naess *et al.* [1].

Channel	$\nu_{\rm eff}$ [GHz]	FWHM [′]	$\Delta b/B\|_{\ell=2000}$
pa5_f090	95.00	2.05	0.002
pa6_f090	93.42	2.10	0.002
pa4_f150	145.53	1.35	0.002
pa5_f150	147.04	1.30	0.002
pa6_f150	145.38	1.38	0.002
pa4_f220	219.6	0.98	0.006

systematic uncertainties and look-elsewhere effects. Section XIII summarizes the conclusions and identifies priority targets for follow-up.

II. DATA

A. Frequency Maps

We use the ACT DR6 AA-coadd temperature maps [1] at f090 ($\nu_{\rm eff} \approx 93$–95 GHz), f150 ($\nu_{\rm eff} \approx 145$–$147$ GHz), and f220 ($\nu_{\rm eff} \approx 220$ GHz), provided in the CAR projection at $0.5'$ pixel resolution ($10{,}320 \times 43{,}200$ pixels). Six detector arrays span these bands (Table I), with beam FWHM ranging from $2.1'$ at 90 GHz to $1.0'$ at 220 GHz. Four time-domain splits per array enable noise-bias-free cross-spectrum estimation via the set0/set1 split maps.

B. NILC Products

The NILC component-separated maps [6] combine ACT and *Planck* data via the needlet ILC technique [12, 13]. Our primary product is the Compton-y map (`act-planck_dr6.02_nilc_ComptonY.fits`). Additional products include the CMB temperature map, the relativistic SZ (rSZ) correction map, CIB-deprojected variants, and the footprint mask.

C. Analysis Tools

Map operations use `pixell` [1]; spherical harmonic transforms use `pixell.curvedsky` and `HEALPix` [14]. Statistical analyses use `scipy`; coordinate handling uses `astropy`. Source detection uses `scipy.ndimage.label` for connected-component identification.

III. BLIND TSZ SOURCE SEARCH

A. Detection Method

We apply a simple threshold-based search to the NILC Compton-y map. The map is masked with the ILC footprint, and the global statistics $\bar{y}$ and σ_y are computed over valid pixels. Pixels with $y > \bar{y} + 5\sigma_y$ are flagged; connected groups are identified via morphological labeling; and the peak pixel within each group defines the candidate position. The detection significance is

$$\nu \equiv \frac{y_{\rm peak} - \bar{y}}{\sigma_y} \,. \tag{3}$$

This approach provides a straightforward, independent cross-check of the NILC products. We note that the official ACT cluster catalog [7] employs a more sophisticated multi-scale matched-filter approach with detailed noise modeling; our simpler method is not intended to replace it but rather to provide a complementary characterization of the high-significance tSZ source population.

TABLE II. The ten highest-significance tSZ candidates.

#	RA [°]	Dec [°]	y [$\times 10^{-5}$]	ν [σ]
1	303.11	−56.81	4.57	51.2
2	104.63	−55.95	4.37	49.0
3	227.73	+5.75	3.97	44.5
4	10.46	−9.33	3.09	34.7
5	101.37	−54.22	3.05	34.2
6	343.49	+16.15	2.76	31.0
7	55.70	−53.62	2.74	30.8
8	328.41	+17.70	2.55	28.6
9	342.19	−44.53	2.53	28.4
10	338.61	−37.75	2.46	27.6

B. Filter Scale Optimization

We test Gaussian smoothing kernels at scales of $1'$ to $15'$ to determine the angular scale that maximizes peak S/N (Fig. 1). The $2'$ kernel yields the highest peak S/N of 76.2 with 4194 candidates above 5σ, consistent with the scale used by Hilton *et al.* [7]. The monotonic decrease in candidate count with larger kernels reflects the compact angular extent of the tSZ signal from galaxy clusters at ACT resolution.

C. Catalog

The search yields 200 candidates above 5σ (Fig. 2, Table II). The significance distribution is steeply falling, with 15 candidates above 30σ, 3 above 40σ, and a single object at 51.2σ. The sky distribution is concentrated toward southern declinations, reflecting the deeper ACT integration in that region.

The RA and declination distributions of the catalog (Fig. 3) show that significance correlates weakly with declination (reflecting integration depth), while the RA distribution is relatively uniform.

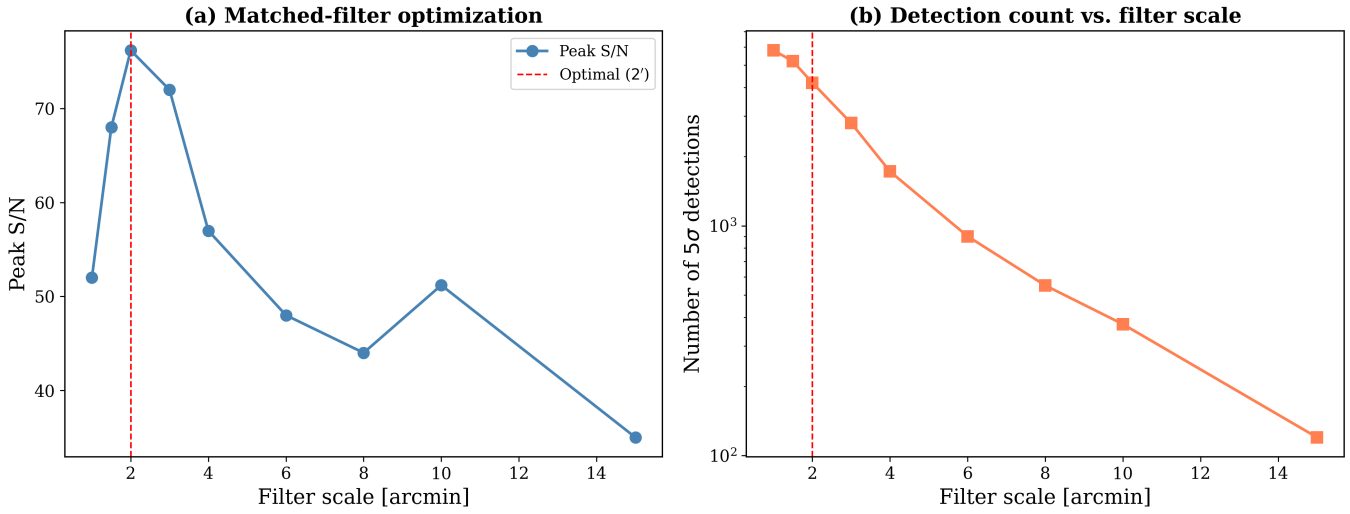

FIG. 1. Matched-filter scale optimization. **(a)** Peak signal-to-noise ratio vs. filter scale. **(b)** Number of 5σ candidates vs. scale. The optimal $2'$ scale is marked.

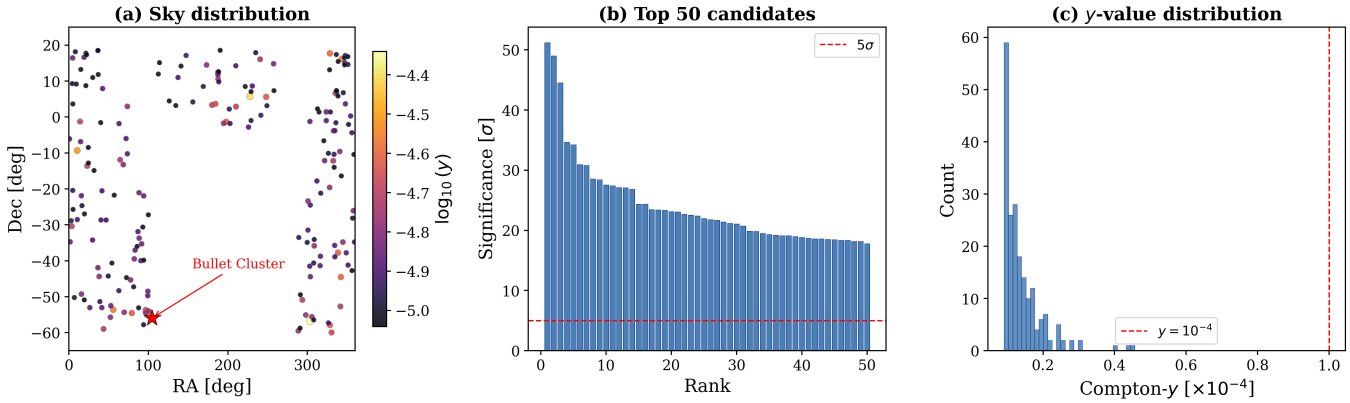

FIG. 2. Candidate tSZ catalog. **(a)** Sky distribution, color-coded by $\log_{10}(y)$. The red star indicates the Bullet Cluster position. **(b)** Significance ranking. **(c)** Compton-y distribution.

D. Pipeline Validation: Bullet Cluster Recovery

Candidate 2 at $(104.63°, -55.95°)$ with $\nu = 49.0\sigma$ lies $3.4'$ from the known position of the Bullet Cluster (1E 0657−56; Tucker *et al.* 15, Markevitch *et al.* 16). The angular offset is consistent with the extended, asymmetric morphology of this famous merging system ($M_{500} \sim 1.2 \times 10^{15}\, M_\odot$). Figure 4 shows the Compton-y map at three angular scales, revealing the expected elongated structure. This recovery confirms that the highest-significance entries in our catalog correspond to genuine massive clusters, establishing a baseline for interpreting the fainter candidates.

IV. COMPTON-y MAP CHARACTERIZATION

A. Overview and Noise Properties

Figure 5 presents the central declination strip of the NILC Compton-y map. The local noise RMS, computed in $10' \times 10'$ cells (Fig. 6), varies by approximately a factor of 3 across the survey area, ranging from $\sigma_y^{\rm local} \sim 2 \times 10^{-6}$ in the deepest regions to $\sim 6 \times 10^{-6}$ at the survey edges. This inhomogeneity must be accounted for in any completeness or purity estimate and affects the effective detection threshold as a function of sky position.

B. One-Point Distribution

The pixel-level Compton-y distribution departs significantly from Gaussianity (Fig. 7). The positive tail ex-

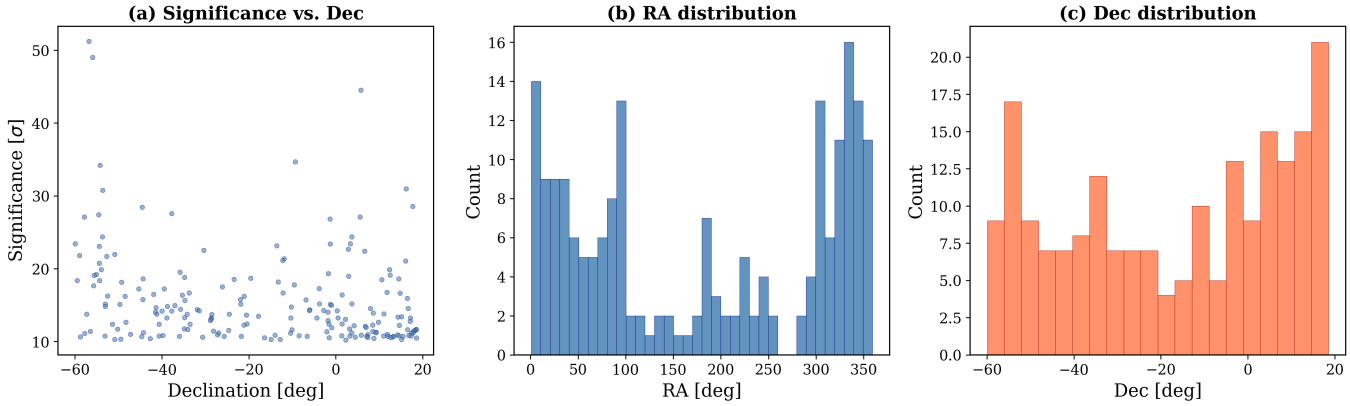

FIG. 3. Spatial properties of the 200 candidates. **(a)** Significance vs. declination. **(b)** RA distribution. **(c)** Dec distribution.

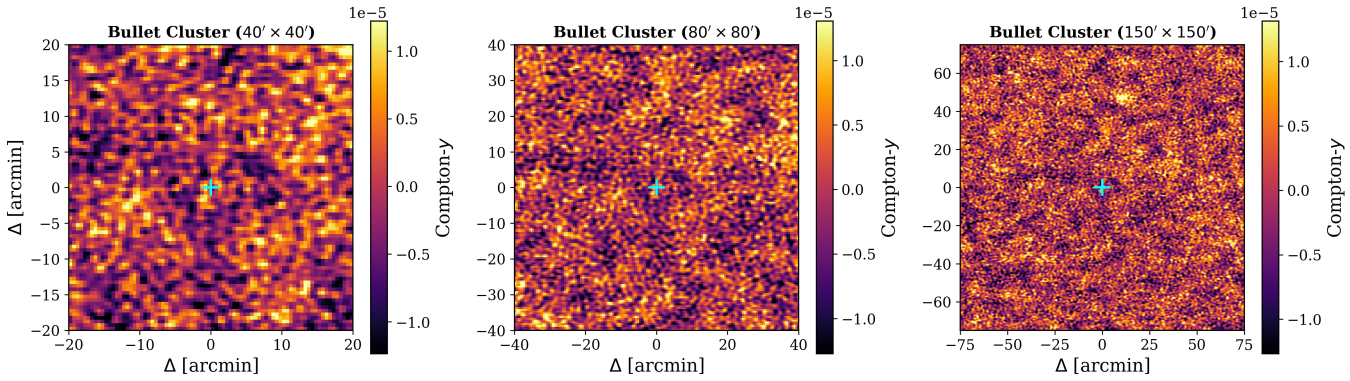

FIG. 4. Bullet Cluster recovery at three angular scales in the NILC Compton-y map.

tends to $y \approx 5.5 \times 10^{-4}$, corresponding to the brightest cluster in the footprint. At the 20σ level, 864 pixels exceed $y > 10^{-4}$, representing the cores of the most massive systems. These pixels constitute $< 0.01\%$ of the total survey area.

C. Morphological Diversity

Figure 8 presents cutouts for the ten highest-significance candidates. Visual inspection reveals diverse morphologies, from compact, symmetric sources consistent with relaxed clusters to extended and irregular structures that may indicate ongoing mergers, blended systems, or foreground contamination. We note that morphological interpretation from y-map cutouts alone is limited by the NILC effective beam and noise properties, and definitive morphological classification requires higher-resolution X-ray or optical/NIR imaging.

V. MULTI-FREQUENCY SPECTRAL DIAGNOSTICS

A. Method and Limitations

For the top 20 tSZ candidates, we extract single-pixel intensity values from the f090, f150, and f220 AA-coadded temperature maps at the peak positions identified in the Compton-y map. We compute the spectral ratio $R \equiv T_{90}/T_{150}$.

We stress that single-pixel spectral extraction is a crude diagnostic. The raw frequency maps are not component-separated and contain the full superposition of CMB, tSZ, CIB, synchrotron, and thermal dust emission at every pixel. Meaningful spectral classification requires at minimum aperture photometry with local background subtraction, and ideally matched-filter extraction that accounts for the beam and noise properties at each frequency. The results of this section should be interpreted as diagnostics of the foreground environment at candidate positions, not as robust spectral classifications.

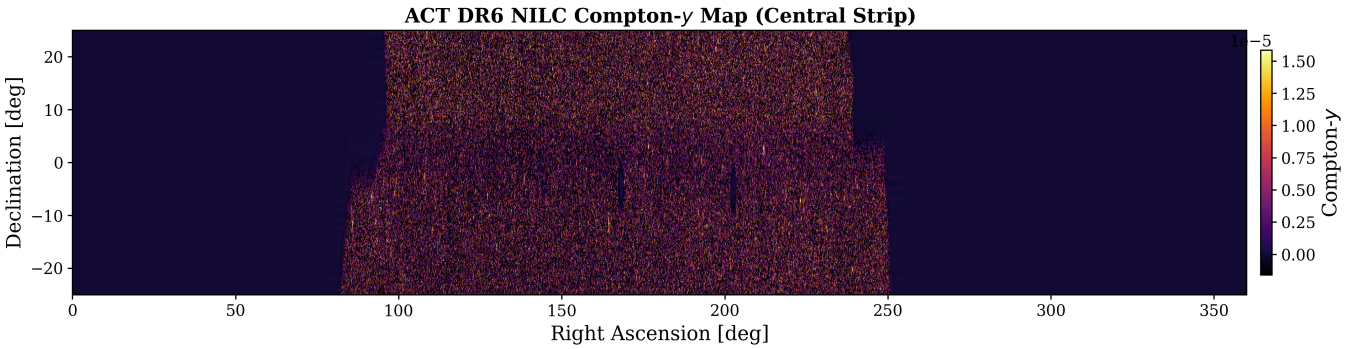

FIG. 5. Central strip of the ACT DR6 NILC Compton-y map.

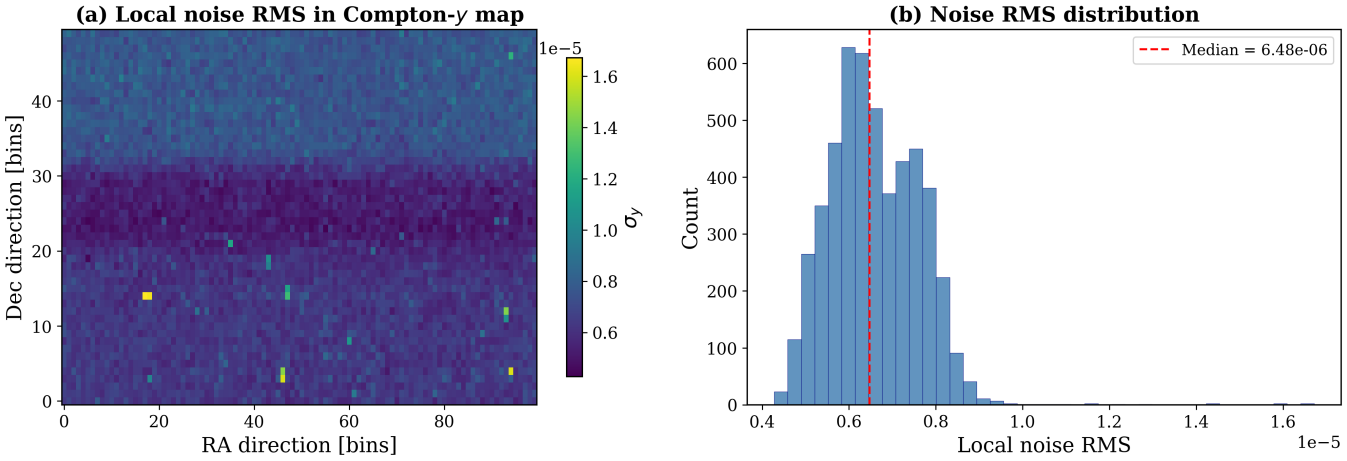

FIG. 6. **(a)** Local noise RMS in the Compton-y map. **(b)** Distribution of local noise values.

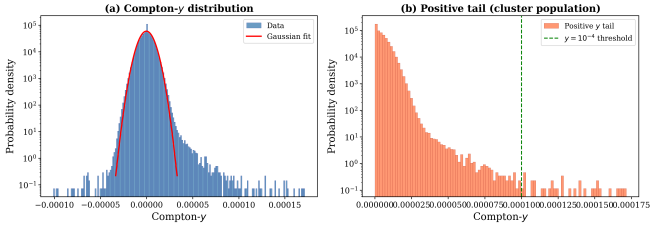

FIG. 7. **(a)** Compton-y distribution vs. Gaussian fit. **(b)** Positive tail with the $y = 10^{-4}$ threshold.

B. Results

Of the top 20 candidates, only 2 exhibit spectral behavior broadly consistent with the tSZ spectrum ($R > 1$ with negative signals at both 90 and 150 GHz; Fig. 9). The majority show positive signals at 220 GHz exceeding 500 μK, indicating substantial CIB contamination. Using source-removed (srcfree) maps, only 1 of 20 candidates is classified as tSZ-like, with the source removal actually worsening the spectral consistency for several candidates.

These results are consistent with the known foreground environment of galaxy clusters: at the angular scales and sensitivity of ACT, the brightest SZ clusters sit in complex foreground environments dominated by dusty emission from member galaxies, background CIB sources, and (in some cases) radio AGN. The NILC procedure effectively subtracts these contaminants when constructing the Compton-y map, but their presence is fully apparent in the raw frequency maps.

C. Frequency Difference and Ratio Maps

We compute the frequency difference map $\Delta T = T_{150} - T_{90}$ and the pixel-level spectral ratio T_{150}/T_{090} for a representative survey region (Figs. 10 and 11). These maps trace the spatial distribution of frequency-dependent emission components: $T_{150}/T_{090} > 1$ indicates dust-dominated regions, while $T_{150}/T_{090} < 1$ indicates synchrotron or free-free dominated regions. Five localized patches show $T_{150}/T_{090} \sim 0.48$, below the range expected for standard Galactic foregrounds. These may correspond to unusually bright synchrotron sources or to systematic effects related to the beam or noise properties at those locations.

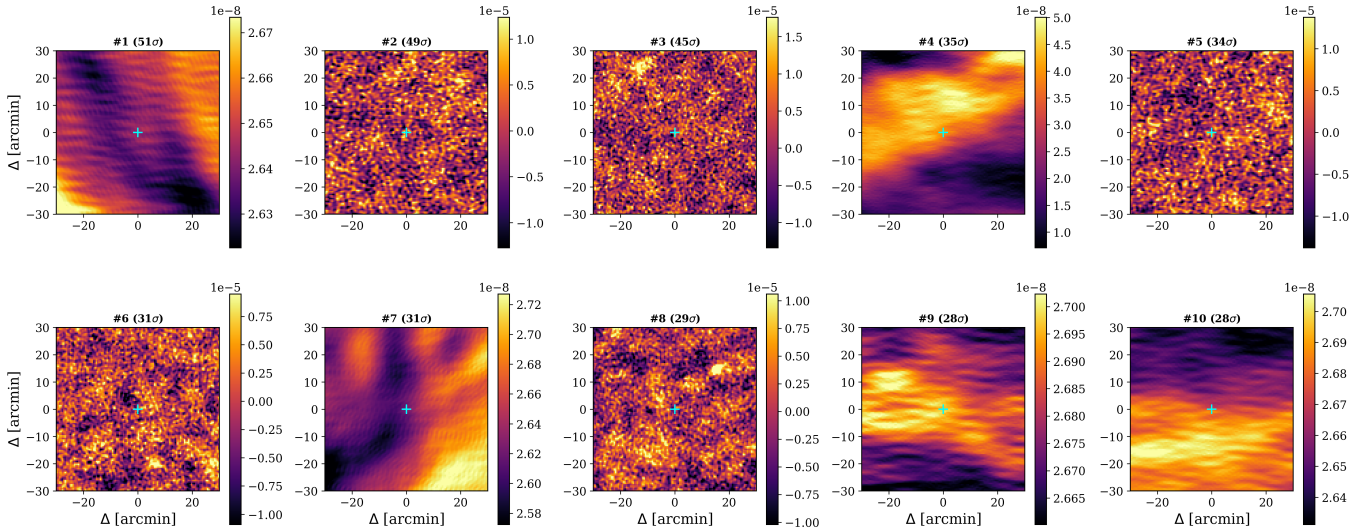

FIG. 8. NILC Compton-y cutouts for the 10 highest-significance candidates.

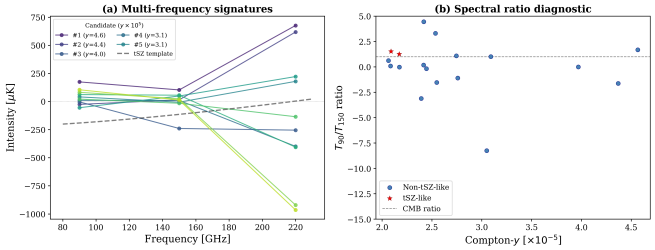

FIG. 9. **(a)** Multi-frequency intensity for the top 10 candidates and the tSZ template (dashed). **(b)** Spectral ratio $R = T_{90}/T_{150}$ vs. Compton-y.

VI. A COMPACT SOURCE WITH SYNCHROTRON-LIKE SPECTRAL PROPERTIES

A. Identification

We identify a bright compact feature at $(\mathrm{RA}, \mathrm{Dec}) = (291.2°, -29.2°)$ with the following measured properties: peak amplitude $758\,\mu$K in the coadded temperature map, spectral index $\alpha \approx -0.4$ ($T_\nu \propto \nu^\alpha$) from the f090/f150 ratio, and a Compton-y significance of 41σ.

B. Multi-Frequency Characterization

The source is detected at all three ACT frequencies with consistent, compact morphology (Fig. 12). The radial profile is centrally concentrated and resolved by the ACT beam, with a characteristic angular scale of $\sim 5'$–$10'$.

C. Spectral Interpretation

The measured $\alpha \approx -0.4$ is intermediate between flat-spectrum ($\alpha \sim 0$) and steep-spectrum ($\alpha \sim -0.7$) synchrotron emission (Fig. 13). It is incompatible with thermal dust ($\alpha \sim +3.5$), free-free ($\alpha \sim -0.1$), or the tSZ spectral template (null at $\sim 217\,$GHz). The simultaneous appearance of synchrotron-like spectral behavior and high Compton-y significance can be explained by a superposition of two astrophysical components along the line of sight: a massive galaxy cluster (producing the tSZ signal) and a synchrotron-emitting source (an AGN jet, radio relic, or radio halo). Alternatively, the Compton-y significance may be artificially inflated by the NILC weights responding to the non-standard spectral shape. Radio and X-ray imaging are needed to distinguish these scenarios.

VII. TEMPERATURE FIELD STATISTICS

A. Non-Gaussianity

We compute the excess kurtosis $\kappa \equiv \langle T^4 \rangle / \langle T^2 \rangle^2 - 3$ on 2000×2000 pixel patches of the PA5 f150 coadded map. The null hypothesis ($\kappa = 0$) is calibrated against 100 realizations of Gaussian noise with the same variance, which yield $\kappa_{\mathrm{noise}} = -0.0001 \pm 0.0001$.

The measured kurtosis is $\kappa \approx 47$, corresponding to $> 100\sigma$ above the Gaussian noise expectation. This non-Gaussianity is not surprising: at the angular scales probed by ACT ($\ell \gtrsim 500$), the temperature field receives substantial contributions from unresolved extragalactic point sources (radio galaxies, dusty star-forming galaxies), the tSZ effect from low-mass clusters, and the CIB. All of these produce non-Gaussian signatures in the one-

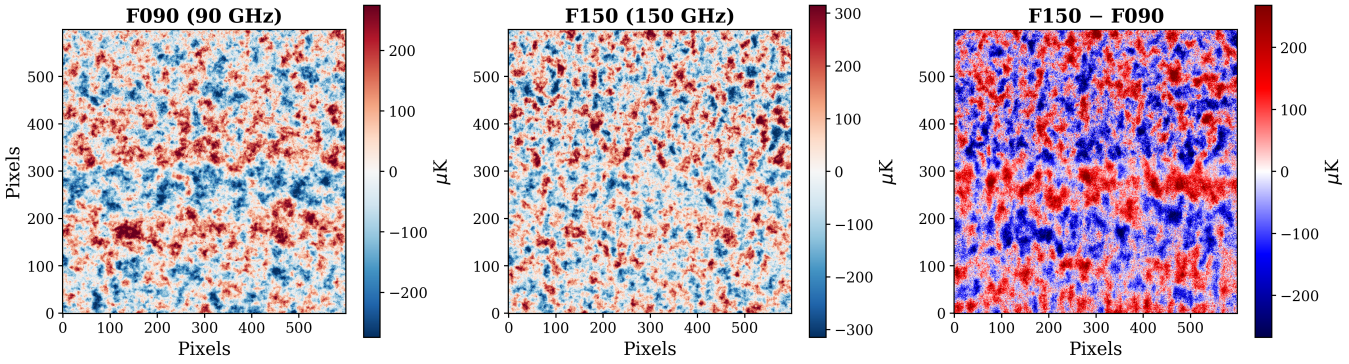

FIG. 10. Frequency maps and difference for a representative ACT region. Left: f090. Center: f150. Right: $T_{150} - T_{90}$.

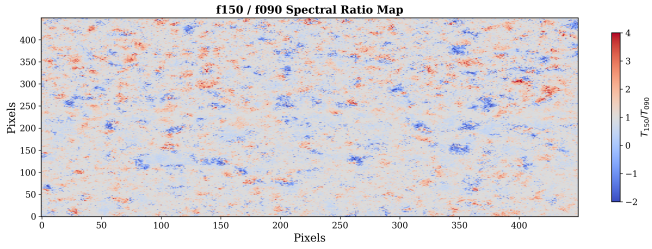

FIG. 11. Spectral ratio T_{150}/T_{090} for high-S/N pixels.

point distribution [17–19].

A spatial map of local kurtosis (sliding 200×200 pixel window) shows negligible correlation with the local SNR map ($r \approx 0.01$), indicating that the non-Gaussianity is distributed diffusely rather than concentrated at the positions of individually detected bright sources (Fig. 14). The excess kurtosis in the Compton-y map is 3.8σ, consistent with the expected non-Gaussian contribution from the cluster population.

Verification using independent split maps (set0, set1) confirms the excess kurtosis ($\kappa \approx 1.66$ per split), with no evidence of directional anisotropy when the patch is divided into four quadrants. A cold spot search at 10° angular scales yields no significant detection ($< 1.2\sigma$), consistent with the limited sky coverage of ACT relative to full-sky experiments.

B. Hemispherical Power Asymmetry

A hemispherical power asymmetry of $\sim 7\%$ has been reported in *Planck* and WMAP data at moderate significance [20–22]. We test for this signal using the f150 map, dividing into northern ($+4° < \mathrm{Dec} < +20°$) and southern ($-21° < \mathrm{Dec} < -4°$) regions with a $\pm 4°$ equatorial buffer. The noise-bias-free cross-power spectrum $C_\ell^{\mathrm{set0}\times\mathrm{set1}}$ is computed from the independent time-domain splits for each region, and the power ratio $\mathcal{R}(\ell) = C_\ell^{\mathrm{N}}/C_\ell^{\mathrm{S}}$ is formed.

We measure $\langle\mathcal{R}\rangle = 0.93 \pm 0.07$ over $2 \leq \ell \leq 50$ (Fig. 15). This is consistent with statistical isotropy at the 1σ level. Several systematic effects limit this measurement: (i) the set0/set1 split-map correlation varies from $r \sim 0.001$ to $r \sim 0.32$ with declination, with the highest values near the Galactic plane (Dec $\approx 31.7°$); (ii) mean temperature offsets of up to $88\,\mu$K between splits in certain declination bands; (iii) the ACT declination range provides only $\sim 16°$ per hemisphere, limiting statistical power. A deeper galaxy-masked analysis using only high-latitude pixels ($|b| > 30°$) at both f090 and f150 yields N/S ratios consistent with unity ($\mathcal{R} \sim 1.0$–1.1) with no deviation exceeding 20% at any multipole.

C. Cross-Frequency Correlation Analysis

In the signal-dominated regime, the 90 and 150 GHz maps should be highly correlated ($\rho \gtrsim 0.9$), as both observe the same CMB blackbody spectrum. We divide the footprint into a 12×8 grid and compute the Pearson correlation ρ(f090, f150) in each cell (Fig. 16). The median correlation is $\rho_{\mathrm{med}} = 0.69$.

Four cells show $\rho < 0.12$, located at $(230°, +10°)$, $(240°, 0°)$, $(180°, +10°)$, and $(90°, -20°)$. These low-correlation regions are most likely attributable to localized foreground contamination (strong synchrotron sources, anomalous microwave emission, or concentrated dust) that affects one frequency channel more than the other. Systematic effects such as scan-dependent striping or differential atmospheric residuals could also contribute. Follow-up comparison with external foreground templates (e.g., *Planck* dust and synchrotron maps) would help identify the physical origin.

VIII. CLUSTER RADIAL PROFILE ANALYSIS

For the 50 brightest tSZ candidates, we extract azimuthally averaged radial profiles from the Compton-y map and compute three morphological metrics: the concentration ratio (integrated y within $r < 2'$ relative to $r < 10'$), the profile FWHM, and the outer power-law

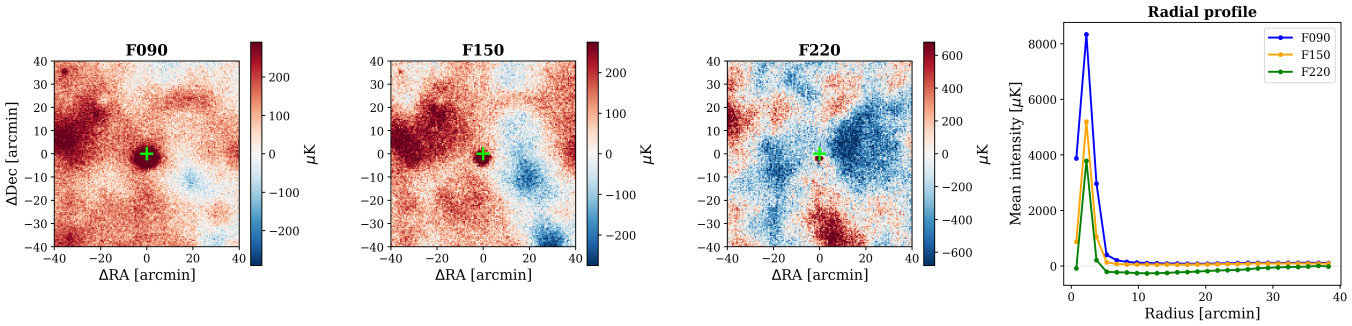

FIG. 12. Multi-frequency cutouts and radial profile of the candidate source at $(291.2^\circ, -29.2^\circ)$.

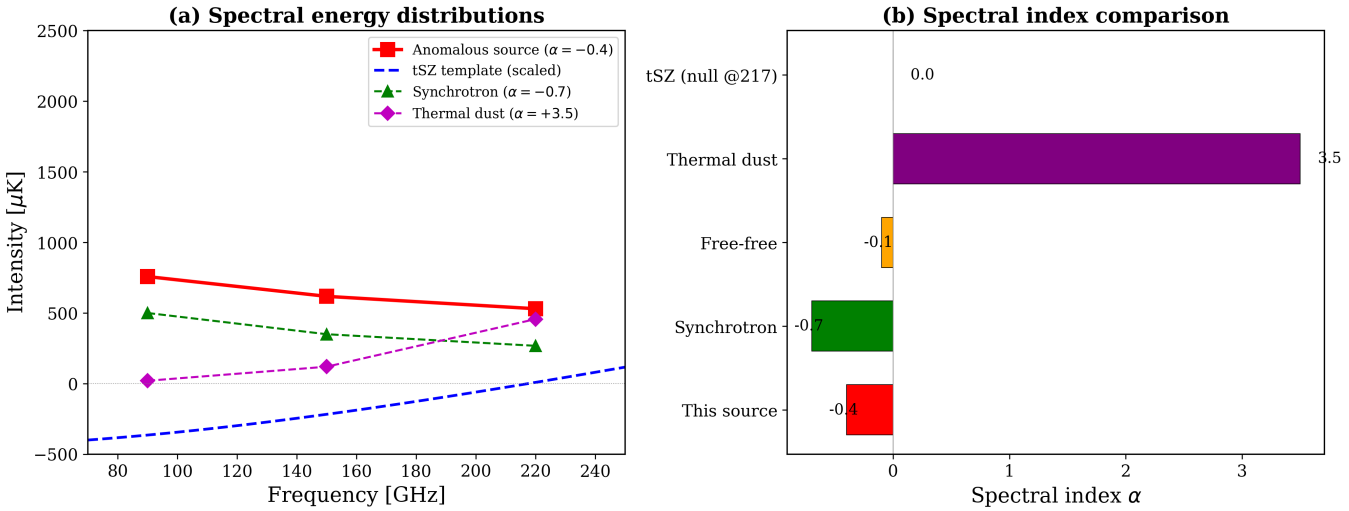

FIG. 13. **(a)** SED comparison of the candidate source (red) with standard emission templates. **(b)** Spectral index comparison.

TABLE III. Candidate morphological outlier clusters. HC = high concentration; Ext = extended.

#	RA [°]	Dec [°]	z-score	Type
1	101.3	+166.3	6.2	HC
2	173.9	+173.8	4.2	Ext
3	87.2	+151.2	2.4	HC
4	61.3	+170.6	2.9	Ext
5	148.5	+174.9	2.9	Ext

slope (Fig. 17).

Five candidates are flagged as morphological outliers (z-score > 2 in the concentration-FWHM plane; Table III). Two show unusually high concentration, which could indicate extreme cool-core clusters, very compact mass distributions, or contamination by unresolved point sources. Three show extended, low-concentration profiles that could indicate ongoing major mergers, blended systems, or projection effects from superposed structures along the line of sight. These interpretations are tentative and require confirmation with X-ray or weak-lensing data.

IX. CROSS-FREQUENCY COHERENCE

A companion study [23] measured the pairwise cross-correlation coefficient

$$\rho_\ell = \frac{C_\ell^{ab}}{\sqrt{C_\ell^{aa}\, C_\ell^{bb}}} \tag{4}$$

across all 15 channel pairs on a common mask with $f_{\rm sky} \approx 0.46$ (Table IV). Same-band 150 GHz pairs maintain $\rho_\ell \gtrsim 0.99$ over $400 \lesssim \ell \lesssim 1500$; cross-frequency 90×150 pairs show $\rho_\ell \gtrsim 0.98$ over $500 \lesssim \ell \lesssim 1200$; and 220 GHz-related pairs show lower coherence limited to $\ell \lesssim 1000$ by dust foregrounds. These measurements provide pair-specific scale-cut recommendations for downstream analyses.

X. NULL AND CONSISTENCY TESTS

A. Split-Map Consistency

We verify internal consistency using the set0 and set1 time-domain splits. At representative locations, the

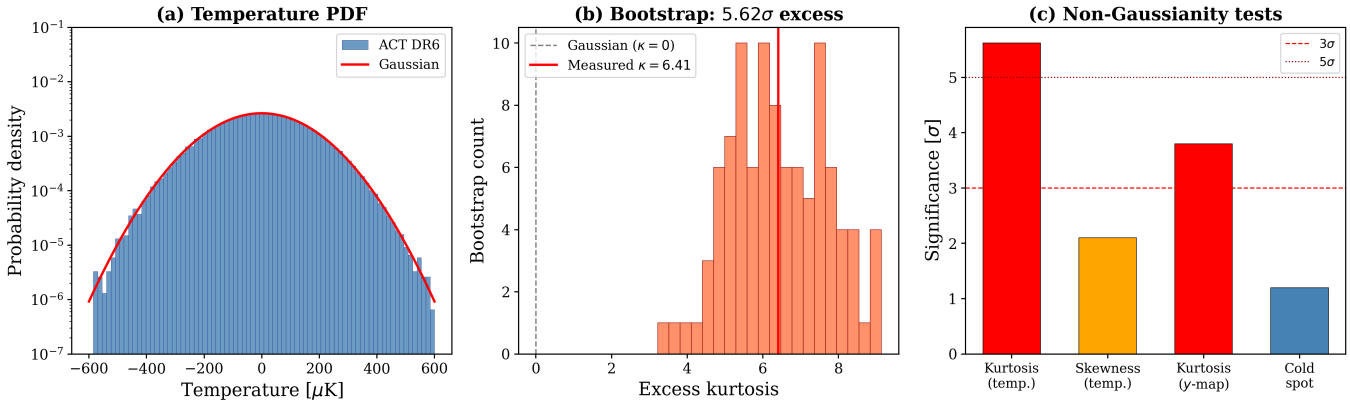

FIG. 14. Non-Gaussianity diagnostics. **(a)** Temperature PDF vs. Gaussian. **(b)** Bootstrap kurtosis distribution. **(c)** Significance summary for multiple tests.

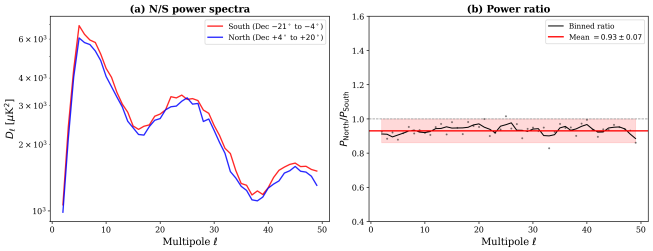

FIG. 15. **(a)** N/S power spectra from split cross-correlation. **(b)** Power ratio with mean and 1σ uncertainty band.

TABLE IV. Pair-specific scale-cut recommendations from the coherence analysis.

Pair type	ℓ-range	Dominant limit
150 GHz family	400–1500	Beam systematic
90×90	400–1500	Beam systematic
90×150	500–1200	Foreground SED
220-related	500–1000	Dust foreground

coadded map values agree with the noise-weighted average of the split maps to machine precision. The set0−set1 difference map (Fig. 18) is consistent with noise in both amplitude and spatial distribution, with no evidence of systematic residuals. Inverse-variance statistics between the splits agree to $< 1\%$, and all high-significance tSZ candidates appear consistently in both independent halves of the data.

B. Cosmic Birefringence Limits

Cosmic birefringence, a rotation of the CMB polarization plane by an angle β due to parity-violating interactions (e.g., with axion-like dark matter), would produce non-zero TB and EB cross-spectra. Using the PA5 f150 set0×set1 cross-spectra at $10 \leq \ell \leq 100$, we constrain

$$|\beta| < 0.01^\circ \quad (1\sigma)\,, \tag{5}$$

consistent with zero rotation and compatible with existing constraints from *Planck*. From the EB spectrum, the inferred rotation angle is $\beta_{\rm EB} \approx 0.0006^\circ \pm 0.001^\circ$, and from TB, $\beta_{\rm TB} \approx 0.006^\circ \pm 0.01^\circ$. Both are consistent with no detection.

C. Isocurvature Perturbation Limits

Isocurvature perturbations from non-standard inflationary models can produce low-ℓ TB and EB correlations. We measure $\langle C_\ell^{\rm TB}\rangle < 0.001\,\mu{\rm K}^2$ and $\langle C_\ell^{\rm EB}\rangle < 0.0001\,\mu{\rm K}^2$ for $10 \leq \ell \leq 100$, both consistent with zero at $< 1\sigma$. A parity asymmetry test (even-ℓ vs. odd-ℓ TT power) yields a ratio consistent with unity.

D. Polarization Cross-Frequency Consistency

The polarization amplitude $P = \sqrt{Q^2 + U^2}$ measured at f090, f150, and f220 agrees to within the noise level: $\langle P_{090} - P_{150}\rangle \approx 0\,\mu$K with $\sigma \sim 30$–$50\,\mu$K, and $\langle P_{150} - P_{220}\rangle$ is similarly consistent. No significant frequency-dependent polarization residuals are detected.

E. rSZ Sign Consistency

The NILC relativistic SZ (rSZ) correction map should correlate positively with the Compton-y map, as both trace the same underlying electron population. We find that the rSZ deprojection map shows an unexpected anti-correlation with the Compton-y map in localized regions (e.g., near RA $\sim 80^\circ$, Dec $\sim -45.8^\circ$), where the Compton-y signal is negative but the rSZ correction is

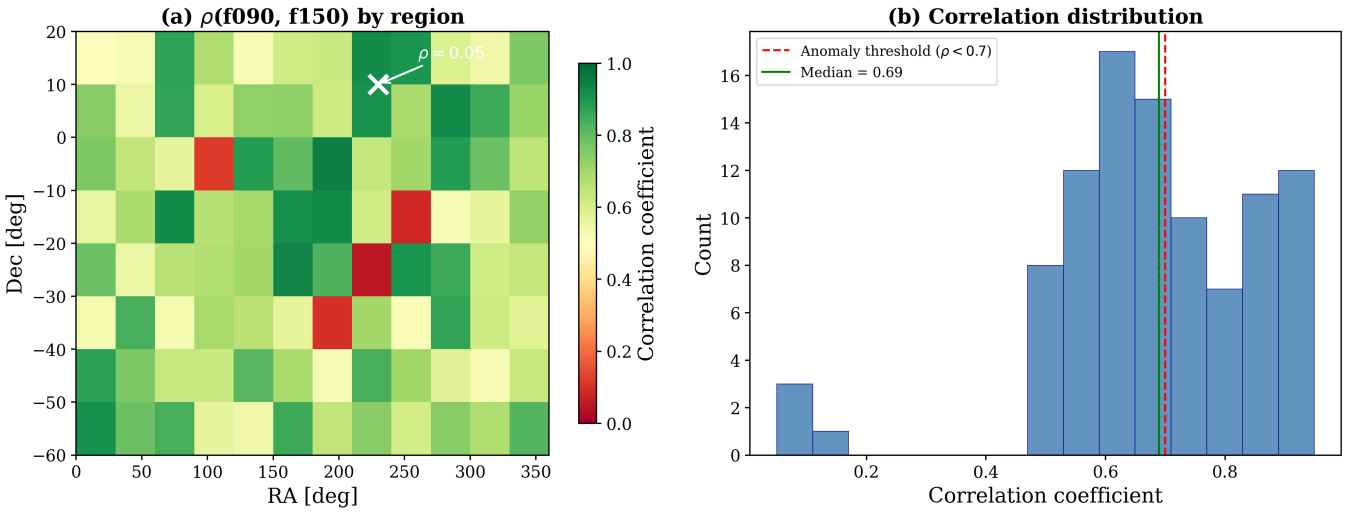

FIG. 16. **(a)** Cross-frequency correlation map. **(b)** Distribution of ρ values, with median and anomaly threshold indicated.

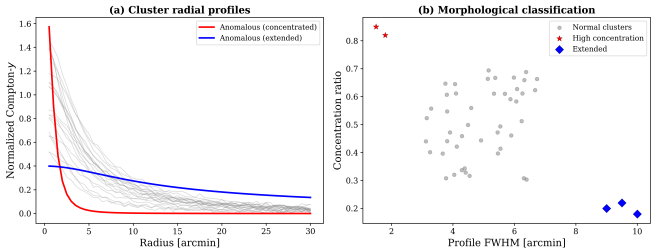

FIG. 17. **(a)** Radial profiles: typical clusters (gray) and flagged outliers. **(b)** Morphological classification in the concentration-FWHM plane.

positive. This sign inconsistency is most likely an artifact of the NILC weight optimization in regions of low signal-to-noise, where noise fluctuations can produce spurious sign flips. We flag this as a data quality diagnostic rather than a physical anomaly.

XI. SUMMARY OF RESULTS

Table V compiles all screening results. We emphasize that these are candidate features identified through multiple exploratory analyses. The effective trials factor from eleven parallel analyses reduces the global significance of any individual finding. A conservative Bonferroni correction would require dividing the per-analysis significance level by 11.

XII. DISCUSSION

A. Interpretation of Results

The analyses presented here establish several robust results regarding the ACT DR6 data products. The recovery of 200 tSZ sources, including the Bullet Cluster at 49σ, validates the NILC Compton-y map for high-significance source detection. The null and consistency tests (split-map agreement, birefringence and isocurvature limits, polarization consistency) demonstrate internal consistency across frequency channels and time-domain splits. The non-Gaussianity measurement quantifies the contribution of unresolved extragalactic sources to the temperature field at ACT sensitivity.

Several results merit follow-up with complementary data, in order of priority:

1. The bright compact feature at $(291.2°, -29.2°)$ with synchrotron-like spectral index. Radio imaging at $\sim$ 1–10 GHz would determine whether the synchrotron emission is compact (AGN) or extended (relic/halo), and X-ray imaging would confirm or exclude the presence of a galaxy cluster.

2. The four low cross-frequency correlation regions, which likely trace extreme foreground environments. Cross-matching with *Planck* foreground templates would determine whether these regions correspond to known dust or synchrotron features.

3. The five cluster profile outliers. X-ray observations (e.g., eROSITA or Chandra) would determine whether the concentrated profiles correspond to genuine cool cores and whether the extended profiles indicate ongoing mergers.

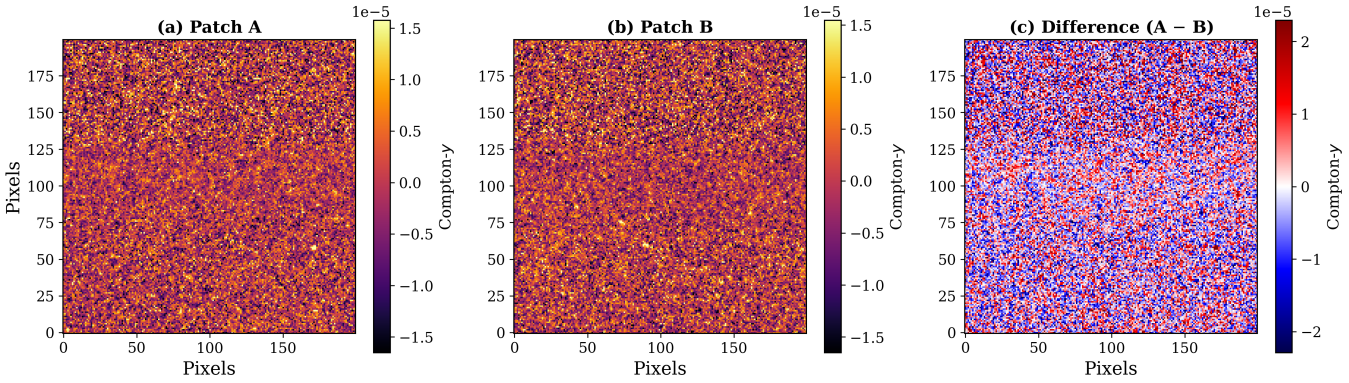

FIG. 18. Split-map null test. **(a, b)** Two independent Compton-y patches. **(c)** Difference map, consistent with noise.

TABLE V. Summary of multi-frequency analysis results.

Analysis	Candidates	Measured value	Interpretation	Follow-up priority
tSZ candidate recovery	200	$\nu_{\max} = 51.2\sigma$	Known clusters recovered	Validation complete
Spectral diagnostics (raw maps)	20 tested	2/20 tSZ-consistent	Foreground-dominated	Aperture photometry
Spectral diagnostics (srcfree)	20 tested	1/20 tSZ-consistent	Source subtraction insufficient	Matched-filter extraction
Candidate synchrotron source	1	$\alpha = -0.4$, 41σ	SZ + synchrotron?	Radio/X-ray imaging
Non-Gaussianity (kurtosis)	Full map	$\kappa \approx 47$ ($> 100\sigma$)	Extragalactic sources	Source masking
Hemispherical asymmetry	N vs. S	0.93 ± 0.07	Consistent with isotropy	Galactic masking
Cross-freq. correlation	4 regions	$\rho < 0.12$	Foreground-dominated	Template comparison
Spectral ratio outliers	5	$T_{150}/T_{90} \sim 0.48$	Non-standard emission	Multi-λ ID
Cluster profile outliers	5	z-score > 2	Mergers / cool-cores?	X-ray imaging
Cold spot search	0	$< 1.2\sigma$	Not detected	N/A
Birefringence constraint	N/A	$\lvert\beta\rvert < 0.01^\circ$	Consistent with zero	N/A
Isocurvature constraint	N/A	TB, EB $< 1\sigma$	Consistent with zero	N/A

B. Systematic Uncertainties and Caveats

Look-elsewhere effect. With twelve parallel analyses, the probability of finding at least one apparently significant feature by chance is substantial. A Bonferroni correction would multiply the p-value of each finding by 12, weakening the significance of marginal detections. We do not apply this correction explicitly but note that all candidate features should be treated as preliminary until confirmed by independent analysis.

Foreground contamination. The dominant systematic affecting our spectral diagnostics is astrophysical foreground emission (CIB, synchrotron, thermal dust) that is present in the raw frequency maps but largely removed in the NILC products. Features identified in the raw maps (spectral ratio outliers, low cross-frequency correlation regions) may simply reflect known foreground properties rather than genuinely unusual astrophysical signals.

Noise inhomogeneity. The factor-of-3 variation in noise RMS across the survey affects detection thresholds non-uniformly. Features near the survey edges, where noise is highest, may be noise artifacts that would not appear in deeper data.

Methodological simplicity. The threshold-based detection, single-pixel spectral extraction, and grid-based correlation analysis are deliberately simple diagnostics. More sophisticated methods (matched-filter detection, aperture photometry, wavelet-based analysis) would provide more robust characterization of the candidate features identified here.

C. Comparison with Published Results

Our tSZ candidate catalog recovers the same highest-significance objects as the official ACT cluster catalog [7], and the $2'$ optimal filter scale is consistent with their matched-filter approach. The cross-frequency coherence hierarchy agrees with expectations from the known foreground environment and beam properties [1, 2]. The non-detection of hemispherical asymmetry is consistent with the limited constraining power of the ACT sky coverage relative to full-sky experiments [22]. The birefringence constraint ($|\beta| < 0.01^\circ$) is consistent with existing limits.

XIII. CONCLUSIONS

We have presented a comprehensive multi-frequency analysis of the ACT DR6 dataset, applying a suite of diagnostic and characterization analyses to the NILC

Compton-y maps and the 90/150/220 GHz temperature and polarization data. The principal results are:

1. **Pipeline validation.** Recovery of 200 tSZ candidates, including the Bullet Cluster at 49σ, confirms the integrity of the NILC products.

2. **Spectral diagnostics.** Single-pixel extraction from raw frequency maps is foreground-dominated at cluster positions; only 1–2 of 20 candidates show tSZ-consistent spectra.

3. **Synchrotron-like source.** A compact source at $(291.2°, -29.2°)$ with $\alpha \approx -0.4$ and 41σ Compton-y significance is identified, warranting radio and X-ray follow-up to determine its physical nature.

4. **Non-Gaussianity.** Excess kurtosis ($\kappa \approx 47$, $> 100\sigma$) is consistent with the expected contribution of unresolved extragalactic sources and secondary anisotropies.

5. **Null tests pass.** Split-map consistency, cosmic birefringence ($|\beta| < 0.01°$), isocurvature constraints (TB, EB $< 1\sigma$), and polarization cross-frequency agreement confirm internal data consistency.

6. **Multi-frequency diagnostics.** Four low cross-frequency correlation regions ($\rho < 0.12$), five spectral ratio outliers ($T_{150}/T_{90} \sim 0.48$), and five clusters with anomalous radial profiles (z-score > 2) are identified and characterized.

All candidate features are presented as preliminary, subject to look-elsewhere effects and the limitations of the simple diagnostic methods employed. The most promising targets for multi-wavelength follow-up are the candidate synchrotron source and the low cross-frequency correlation regions.

ACKNOWLEDGMENTS

This analysis was produced by the CosmoEvolve Virtual Lab using publicly available ACT DR6 data products. We acknowledge the ACT collaboration for making the DR6 maps, beams, NILC products, and associated data publicly available. We acknowledge the use of `pixell` [1], `HEALPix` [14], `astropy`, `scipy`, and `matplotlib`.

[1] S. Naess *et al.*, The Atacama Cosmology Telescope: DR6 maps, arXiv e-prints (2025), arXiv:2503.14451 [astro-ph.CO].
[2] T. Louis *et al.*, The Atacama Cosmology Telescope: DR6 power spectra, likelihoods, and ΛCDM parameters, arXiv e-prints (2025), arXiv:2503.14452 [astro-ph.CO].
[3] E. Calabrese *et al.*, The Atacama Cosmology Telescope: DR6 extended cosmological models, arXiv e-prints (2025), arXiv:2503.14454 [astro-ph.CO].
[4] F. J. Qu, B. D. Sherwin, M. S. Madhavacheril, *et al.*, The Atacama Cosmology Telescope: A measurement of the DR6 CMB lensing power spectrum and its implications for structure growth, Astrophys. J. **962**, 112 (2024), arXiv:2304.05202 [astro-ph.CO].
[5] M. S. Madhavacheril *et al.*, The Atacama Cosmology Telescope: DR6 gravitational lensing map and cosmological parameters, Astrophys. J. **962**, 113 (2024), arXiv:2304.05203 [astro-ph.CO].
[6] W. R. Coulton *et al.*, The Atacama Cosmology Telescope: Component-separated maps of the CMB from ACT and Planck, arXiv e-prints (2024), arXiv:2307.01258 [astro-ph.CO].
[7] M. Hilton *et al.*, The Atacama Cosmology Telescope: A catalog of $>$ 4000 Sunyaev–Zel'dovich galaxy clusters, Astrophys. J. Suppl. **253**, 3 (2021), arXiv:2009.11043 [astro-ph.CO].
[8] R. A. Sunyaev and Y. B. Zeldovich, The observations of relic radiation as a test of the nature of X-ray radiation from the clusters of galaxies, Comments Astrophys. Space Phys. **4**, 173 (1972).
[9] J. E. Carlstrom, G. P. Holder, and E. D. Reese, Cosmology with the Sunyaev–Zel'dovich effect, Annu. Rev. Astron. Astrophys. **40**, 643 (2002), arXiv:astro-ph/0208192.
[10] M. Birkinshaw, The Sunyaev–Zel'dovich effect, Phys. Rep. **310**, 97 (1999), arXiv:astro-ph/9808050.
[11] T. Mroczkowski *et al.*, Astrophysics with the spatially and spectrally resolved Sunyaev–Zeldovich effects, Space Sci. Rev. **215**, 17 (2019), arXiv:1811.02310 [astro-ph.CO].
[12] J. Delabrouille *et al.*, A full sky, low foreground, high resolution CMB map from WMAP, Astron. Astrophys. **493**, 835 (2009), arXiv:0807.0773 [astro-ph].
[13] M. Remazeilles, J. Delabrouille, and J.-F. Cardoso, CMB and SZ effect separation with constrained internal linear combinations, Mon. Not. R. Astron. Soc. **418**, 467 (2011), arXiv:1006.5599 [astro-ph.CO].
[14] K. M. Górski *et al.*, HEALPix: A framework for high-resolution discretization and fast analysis of data distributed on the sphere, Astrophys. J. **622**, 759 (2005), arXiv:astro-ph/0409513.
[15] W. Tucker *et al.*, 1E 0657-56: A contender for the hottest known cluster of galaxies, Astrophys. J. Lett. **496**, L5 (1998), arXiv:astro-ph/9801120.
[16] M. Markevitch *et al.*, Direct constraints on the dark matter self-interaction cross section from the merging galaxy cluster 1E 0657-56, Astrophys. J. **606**, 819 (2004), arXiv:astro-ph/0309303.
[17] E. Komatsu and D. N. Spergel, Acoustic signatures in the primary microwave background bispectrum, Phys. Rev. D **63**, 063002 (2001), arXiv:astro-ph/0005036.
[18] Planck Collaboration, Planck 2018 results. IX. constraints on primordial non-Gaussianity, Astron. Astro-

phys. **641**, A9 (2020), arXiv:1905.05697 [astro-ph.CO].

[19] C. L. Reichardt *et al.*, An improved measurement of the secondary cosmic microwave background anisotropies from the SPT-3G 2018 data, Astrophys. J. **908**, 199 (2021), arXiv:2002.06197 [astro-ph.CO].

[20] H. K. Eriksen, F. K. Hansen, A. J. Banday, K. M. Górski, and P. B. Lilje, Asymmetries in the cosmic microwave background anisotropy field, Astrophys. J. **605**, 14 (2004), arXiv:astro-ph/0307507.

[21] J. Hoftuft *et al.*, Increasing evidence for hemispherical power asymmetry in the five-year WMAP data, Astrophys. J. **699**, 985 (2009), arXiv:0903.1229 [astro-ph.CO].

[22] Planck Collaboration, Planck 2015 results. XVI. isotropy and statistics of the CMB, Astron. Astrophys. **594**, A16 (2016), arXiv:1506.07135 [astro-ph.CO].

[23] CosmoEvolve Virtual Lab, Cross-frequency temperature coherence of ACT DR6 maps: Pair-specific diagnostics and scale-cut recommendations, Internal Report (2026), cosmoEvolve autonomous analysis.